ACS APPLIED MATERIALS & INTERFACES

Research Article

www.acsami.org

Bimetallic Carbides-Based Nanocomposite as Superior Electrocatalyst for Oxygen Evolution Reaction

Yu-Jia Tang,[‡] Chun-Hui Liu,[‡] Wei Huang, Xiao-Li Wang, Long-Zhang Dong, Shun-Li Li,* and Ya-Qian Lan*

Jiangsu Collaborative Innovation Centre of Biomedical Functional Materials, Jiangsu Key Laboratory of New Power Batteries, School of Chemistry and Materials Science, Nanjing Normal University, Nanjing 210023, China

Supporting Information

ABSTRACT: The development of highly efficient and low-cost oxygen evolution electrocatalysts is extremely imperative for the new energy technology. Transition metal carbides have been investigated as remarkable hydrogen evolution reaction (HER) electrocatalysts but undesired oxygen evolution reaction (OER) electrocatalysts and need further study. Here, a cobalt−molybdenum-based bimetallic carbide coated by N-doped porous carbon and anchored on N-doped reduced graphene oxide film ($Co_6Mo_6C_2$/NCRGO) is synthesized by directly carbonizing the Co-doped polyoxometalate/conductive polymer/graphene oxide (Co-PCG) precursors. The precise control of the Co/Mo molar ratio in the Co-PCG precursor is of critical importance to synthesize pure phase bimetallic carbide of $Co_6Mo_6C_2$. As the highly active and robust OER electrocatalyst, the $Co_6Mo_6C_2$/NCRGO composite exhibits excellent activity in alkaline solution, affording a low overpotential of 260 mV versus RHE at 10 mA cm^{-2}, a small Tafel slope of 50 mV dec^{-1}, as well as long-term stability. The superior OER performances are strongly associated with the active $Co_6Mo_6C_2$ particles, polypyrrole (PPy)-derived N-doped porous carbon, and the conductive RGO films. Remarkably, it is the first evidence that the bimetallic carbides were used as the OER catalysts with such high OER activity.

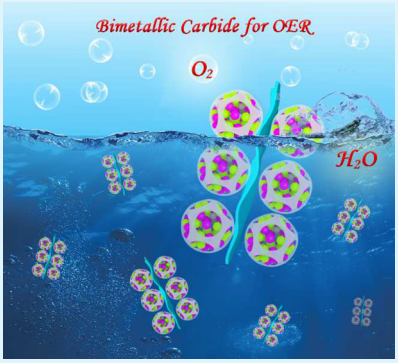

KEYWORDS: *bimetallic carbide, $Co_6Mo_6C_2$, polyoxometalate, PCG, oxygen evolution reaction*

1. INTRODUCTION

Because of the sharp depletion of global energy and the environmental problems that followed, energy consumption is gradually moved from the scarce fossil fuels to the clean and sustainable energy sources.[1,2] Overall water splitting by the electrochemical method has been considered as a promising and eco-friendly candidate to produce renewable hydrogen (H_2) and oxygen (O_2) simultaneously.[3−5] Hydrogen evolution reaction (HER) can easily take place at a low overpotential on many reported non-noble electrocatalysts, which can even replace the commercial Pt-based materials. However, oxygen evolution reaction (OER), as the bottleneck in water splitting, is complex with sluggish kinetics to generate O_2. In general, the overpotential much higher than the theoretical thermodynamic potential value of 1.23 V versus reversible hydrogen electrode (RHE) is needed to expedite the four-electron OER.[6−8] Therefore, the highly efficient and low-cost OER electrocatalysts are required urgently to reduce the overpotential derived from the reaction barriers as well as other resistances and further accelerate the reaction kinetics. Recently, great effort has been made to exploit cost-effective transition metal (e.g., Co, Fe, Ni, and Mo)-based materials as the substitutes of commercial IrO_2 or RuO_2 benchmark for OER, such as transition metal oxides (Co_3O_4/C,[9] MnO_2,[10] and CoMnO[11]), hydroxides (NiCo LDH,[12] and nNiFe LDHs[13]), and phosphides (Ni_2P,[14] CoP,[15] and CoMnP[16]). Nevertheless, these OER catalysts still require high overpotential and suffer some industrial problems, including complex synthetic steps, low yields, and possible aggregation.

Transition metal carbides (TMCs) possess high electron conductivity, metallic property and chemical stability, which has attracted wide interest in the catalytic reaction in early studies, such as the methanol steam reforming[17,18] and oxygen reduction reaction (ORR).[19−22] Recently, TMCs-based materials, especially molybdenum carbides (Mo_2C),[23−27] have emerged as the low-cost and well-established electrocatalysts toward HER in acidic solution but rare as OER catalysts. Only a few studies have discussed their OER properties, while TMCs-based materials still require high overpotential and large Tafel slope because of the agglomeration structure derived from the high-temperature synthesis and instability in the harsh electrolyte.[28−30] Notably, bimetallic carbides-based materials are supposed to be the considerable candidate as the water splitting electrocatalysts because the incorporation of a secondary metal into TMCs can manipulate the electronic structure and expose abundant active sites.[31−34] Therefore, bimetallic carbides could be the promising electrocatalytic alternatives to enhance the OER activity. However, the

Received: January 22, 2017
Accepted: May 5, 2017
Published: May 5, 2017

DOI: 10.1021/acsami.7b01096
ACS Appl. Mater. Interfaces 2017, 9, 16977−16985

preparation of pure phase TMCs, especially the bimetallic carbides, are extremely difficult because the synthesis conditions including the high-temperature calcination usually result in the formation of mixed carbide products. Therefore, it is still a great challenge to prepare the pure phase TMCs using a mild synthesis method.

To further improve the activity and stability of TMCs-based materials, hybridizing nanomaterials of TMCs with graphene, carbon nanotubes (CNTs), and other mesoporous carbon substrates has been reported as a potential method for HER and ORR.[26] TMCs encapsulated in porous carbon could make sure of stability in harsh solution, which can effectively prevent the TMCs from the electrolyte corrosion and prolong the stability tests during the catalytic process. Moreover, these carbon-based materials have high electrical conductivity, large surface area, and unique structures as substrates for OER or HER catalysis.[35] At this point, controlling synthesis of TMCs and in situ hybridization into conductive carbon-based substrates could be an effective method to enhance the electrocatalytic activity and stability for water splitting.

Motivated by these predictions, we have synthesized a pure phase Co−Mo-based bimetallic carbide ($Co_6Mo_6C_2$) coated by N-doped porous carbon and anchored on N-doped reduced graphene oxide, namely $Co_6Mo_6C_2$/NCRGO, via the precise control of the Co/Mo molar ratios in Co-doped polyoxometalates/conductive polymer/graphene oxide (Co-PCG) precursors for the first time.[36] PCG precursors can be synthesized in quantity using a benign hydrothermal method. $H_3PMo_{12}O_{40}\cdot nH_2O$ (PMo_{12}), as a famous Keggin type heteropolyanions of polyoxometalates (POMs), has many advantages of strong redox ability, water solubility, and nanosized structure, which can be dispersed around GO films in water uniformly.[37] After introducing pyrrole (Py) monometer into PMo_{12}/GO solution, spherical-shaped polypyrrole (PPy) can be grown on the surface of GO films because of the hydrothermal condition and the redox ability of PMo_{12}. Simultaneously, PPy can encase PMo_{12} particles around GO films during in situ polymerization. What's more, doping transition metal ion into PCG precursor can provide rich metal sources without morphology or structure change. Metal-doped PCG precursor as the platform for further calcination treatment could be an intriguing strategy to synthesize the bimetallic carbides-based materials without agglomeration. Therefore, as-prepared pure phase $Co_6Mo_6C_2$/NCRGO composite derived from Co-PCG precursor possesses highly active species, large surface area, tunable electronic structures, and approachable mass/charge diffusion pathways. As the OER electrocatalyst, a $Co_6Mo_6C_2$/NCRGO composite shows an ultralow overpotential of 260 mV versus RHE at 10 mA cm^{-2}, Tafel slope of 50 mV dec^{-1}, and long-term stability in alkaline medium. The excellent OER properties could be attributed to the synergetic effects of active $Co_6Mo_6C_2$, N-doped porous carbon, and conductive RGO substrates. To the best of our knowledge, $Co_6Mo_6C_2$/NCRGO composite exhibits the best OER performance among all reported TMCs-based electrocatalysts.

2. EXPERIMENTAL SECTION

Synthesis of $Co_6Mo_6C_2$/NCRGO Nanocomposite and Other Control Samples. GO films were prepared by chemical oxidation exfoliation of graphite using a modified Hummers method.[38] First, 25 mg GO films were dissolved in 25 mL deionized water by ultrasonication to form a suspension with the concentration of 1 mg mL^{-1}. Then, 0.765 g $Co(NO_3)_2\cdot 6H_2O$ (2.6 mmol) and 0.2 g $H_3PMo_{12}O_{40}\cdot nH_2O$ (PMo_{12}, 0.11 mmol) (Co/Mo molar ratio = 2:1) were added into the above suspension to form a homogeneous mixture solution A. 80 μL Py monomer was dispersed in 15 mL deionized water by ultrasonication to produce a mixture solution B. Solution B was transferred into solution A dropwise and then the mixed solution was transferred into a 50 mL Teflon-lined stainless steel autoclave for hydrothermal reaction at 180 °C for 12 h. After cooling down to room temperature, the resulting product of Co-PCG precursor was collected by filtration and washed with deionized water for several times and dried at 60 °C overnight. To prepare the $Co_6Mo_6C_2$/NCRGO nanocomposite, 1 g Co-PCG precursor was annealed directly in a horizontal furnace at 800 °C for 3 h with the heating rate of 5 °C min^{-1} under a nitrogen flow. Co/$Co_6Mo_6C_2$/Mo_2C/NCRGO and $Co_6Mo_6C_2$/Co_6Mo_6C/NCRGO were synthesized through a similar procedure except for the Co/Mo molar ratio being changed to 1:1 and 3:1, respectively. Co/$Co_6Mo_6C_2$/Mo_2C/NCRGO composite was prepared using 0.384 g $Co(NO_3)_2\cdot 6H_2O$ (1.32 mmol), 0.2 g PMo_{12} (0.11 mmol), and 80 μL Py. $Co_6Mo_6C_2$/Co_6Mo_6C/NCRGO composite was prepared using 1.15 g $Co(NO_3)_2\cdot 6H_2O$ (3.96 mmol), 0.2 g PMo_{12} (0.11 mmol), and 80 μL Py. Besides, for a control experiment, $Co_6Mo_6C_2$/NCRGO-1 composite was prepared using ammonium molybdate tetrahydrate ($(NH_4)_6Mo_7O_{24}\cdot 4H_2O$) as a Mo source.

Material Characterization. Powder X-ray diffraction (PXRD) patterns were recorded on a D/max 2500VL/PC diffractometer (Japan) equipped with graphite monochromatized Cu Kα radiation (λ = 1.54060 Å). Corresponding work voltage and current is 40 kV and 100 mA, respectively. Transmission electron microscopy (TEM) image was carried out on JEOL-2100F apparatus at an accelerating voltage of 200 kV. High-resolution TEM (HRTEM) image was carried out on FEI Tecnai G2 F30 apparatus at an accelerating voltage of 300 kV. Surface morphologies of the corresponding samples were examined by a scanning electron microscopy (SEM, JSM-7600F) at an acceleration voltage of 10 kV. Elemental mapping and energy dispersive X-ray spectroscopy (EDX) were performed with JSM-5160LV-Vantage-typed energy spectrometer. X-ray photoelectron spectroscopy (XPS) was collected on scanning X-ray microprobe (PHI 5000 Verasa, ULAC-PHI, Inc.) using Al Kα radiation and the C 1s peak at 284.8 eV as an internal standard. The Raman spectra of dried samples were obtained on Lab-RAM HR800 with excitation by an argon ion laser (514.5 nm). Nitrogen adsorption−desorption isotherms were measured at 77 K on a Quantachrome Instruments Autosorb AS-6B. The pore size distributions were measured by the Barrett−Joyner−Halenda (BJH) method.

Electrochemical Characterization. All electrochemical tests were performed on a CHI 660E electrochemical station (Chenhua, Shanghai, China) in a three-electrode system at room temperature. First, 4 mg of the catalyst was ultrasonically dispersed in the mixture of 1.5 mL water and 0.5 mL ethanol. Then, 5 μL of the catalyst was dropped onto the glassy carbon electrode (GCE, 3 mm in diameter) (loading mass is ~0.14 mg cm^{-2}). After solvent evaporation, 5 μL Nafion solution (0.5 wt %) was coated onto the electrode surface and dried in an ambient environment for measurements. The resulting electrode served as the working electrode. A platinum wire served as a counter electrode and Ag/AgCl (3 M KCl) as the reference electrode. The electrolyte was 1 M KOH and saturated by nitrogen bubbles at least 30 min before the OER measurement. LSV polarization curves were recorded at the scan rate of 5 mV s^{-1}. The working electrodes were scanned for several times until the LSV curves were stabilized, and then the data were collected. The long-term stability was recorded by CV tests between the potential of 0.3 and 0.5 V versus Ag/AgCl at the scan rate of 100 mV s^{-1}. Electrochemical capacitance was determined using CV measurements at the potential range from 0.2 to 0.3 V versus Ag/AgCl at different scan rates (10, 20, 40, 60, 80, and 100 mV s^{-1}). EIS was carried out at the frequency range from 1000 kHz to 100 mHz at the open-circuit voltage. The potential was converted to the reversible hydrogen electrode (RHE) according to the Nernst equation. In 1 M KOH, $E_{RHE} = E_{Ag/AgCl} + 0.205 + 0.059 \times pH$.

DOI: 10.1021/acsami.7b01096
ACS Appl. Mater. Interfaces 2017, 9, 16977−16985

3. RESULTS AND DISCUSSION

Preparation and Characterization of $Co_6Mo_6C_2$/NCRGO Composite. The synthesis route of $Co_6Mo_6C_2$/NCRGO composite is illustrated in Scheme 1. First, Co-PCG precursors were synthesized using a direct hydrothermal method at 180 °C for 12 h by simply mixing $Co(NO_3)_2$, PMo_{12}, Py, and GO films in water. The as-prepared black powder of Co-PCG was transferred into a horizontal furnace and annealed at 800 °C for 3 h in N_2 atmosphere to obtain the final product of $Co_6Mo_6C_2$/NCRGO composite. While the GO concentration (1 mg mL^{-1}) and Py amount (80 μL) remained unchanged, Co−Mo-based composites with different compositions were synthesized through the precise control of Co/Mo molar ratios in Co-PCG precursors (0:1, 1:1, 2:1 to 3:1). First, without Co doping (Co/Mo molar ratio is 0:1), Mo_2C particles coated by N-doped porous carbon and RGO films (Mo_2C/NCRGO) can be obtained by directly carbonizing PCG precursors. After introducing Co sources into PCG precursors with the Co/Mo molar ratio of 1:1, Co/Mo_2C/$Co_6Mo_6C_2$/NCRGO composite with complex compositions was obtained. When tuning the Co/Mo molar ratio to 2:1, $Co_6Mo_6C_2$/NCRGO composite can be synthesized successfully, which has only one kind of pure phase bimetallic carbide of $Co_6Mo_6C_2$ particles. However, further increasing Co amounts to Co/Mo molar ratio of 3:1, another carbide of Co_6Mo_6C with similar structure to $Co_6Mo_6C_2$ appears to form the $Co_6Mo_6C_2$/Co_6Mo_6C/NCRGO composite. Here, the pure phase $Co_6Mo_6C_2$/NCRGO composite prepared with a Co/Mo molar ratio of 2:1 is investigated mainly in the following text due to the simplex composition and excellent OER performance.

Scheme 1. Schematic Diagram for the Synthesis Process of $Co_6Mo_6C_2$/NCRGO Composite

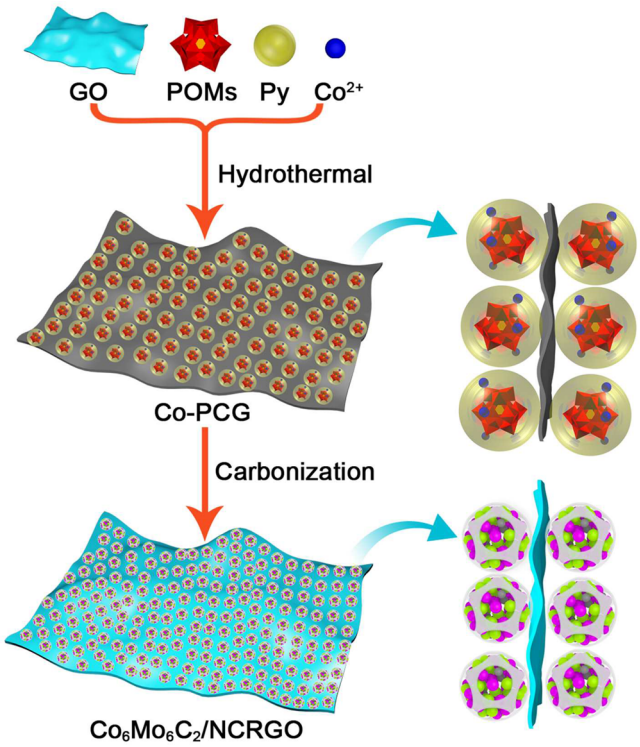

X-ray diffraction (XRD) was used to characterize the structure and crystallinity of Co−Mo-based composites prepared with different Co/Mo molar ratios in Co-PCG precursors. In Figure 1a, $Co_6Mo_6C_2$/NCRGO composite prepared with Co/Mo molar ratio of 2:1 shows a highly crystallized structure with distinct characteristic peaks, which agrees with the $Co_6Mo_6C_2$ phase (JCPDS no. 80-339) with no sign of other carbide species.[39] By contrast, Mo_2C/NCRGO composite without Co doping is matched well with the Mo_2C phase (JCPDS no. 35-787) (Figure S1). When the Co/Mo molar ratio is adjusted to 1:1, the diffraction peaks become diverse with three phases, including Co, Mo_2C, and $Co_6Mo_6C_2$ for a Co/Mo_2C/$Co_6Mo_6C_2$/NCRGO composite (Figure S2). While the Co/Mo molar ratio increased to 3:1, a new Co_6Mo_6C phase (JCPDS no. 65-8115) appears for the $Co_6Mo_6C_2$/Co_6Mo_6C/NCRGO composite, which has a similar peak position to the $Co_6Mo_6C_2$ phase (Figure S3). Besides, $Co_6Mo_6C_2$/NCRGO composites prepared with other GO amounts (0 and 2 mg mL^{-1}) also show the distinct peaks of the $Co_6Mo_6C_2$ phase (Figure S4). On the basis of these results, the formation of pure phase $Co_6Mo_6C_2$ is closely associated with the controlling of Co/Mo molar ratios in Co-PCG precursors.

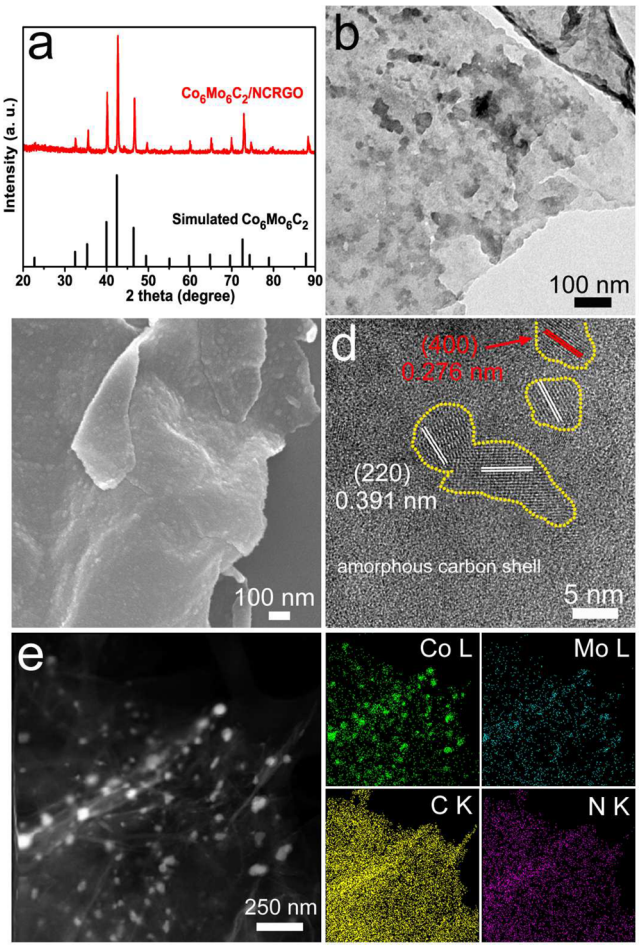

Figure 1. (a) XRD pattern of $Co_6Mo_6C_2$/NCRGO composite, (b) TEM, (c) SEM and (d) HRTEM images of $Co_6Mo_6C_2$/NCRGO composite, (e) HAADF-STEM image and corresponding EDX mapping analysis of Co, Mo, C and N for $Co_6Mo_6C_2$/NCRGO composite.

DOI: 10.1021/acsami.7b01096
ACS Appl. Mater. Interfaces 2017, 9, 16977−16985

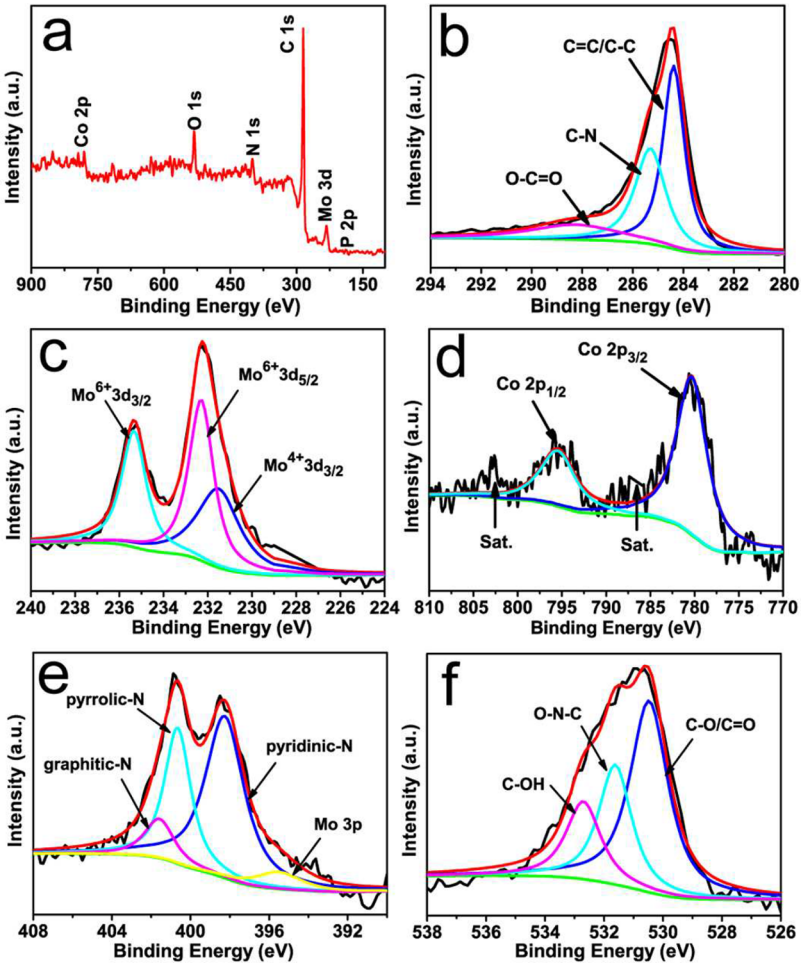

Figure 2. (a) Full scan XPS spectrum of $Co_6Mo_6C_2$/NCRGO composite. High resolution spectra of (b) C 1s, (c) Mo 3d, (d) Co 2p, (e) N 1s, and (f) O 1s.

The morphology and structure of Co−Mo-based composites were further characterized by transmission electron microscopy (TEM) and scanning electron microscopy (SEM). TEM image of $Co_6Mo_6C_2$/NCRGO composite (Figure 1b) shows that monodisperse $Co_6Mo_6C_2$ nanoparticles coated by porous carbon with a size range of 20−50 nm are tightly grown on RGO substrates uniformly. SEM image (Figure 1c) demonstrates that fold RGO nanosheets are decorated with spherical porous carbon uniformly. TEM and SEM images of Co−Mo-based composites prepared with other Co/Mo molar ratios (0:1, 1:1 and 3:1) exhibit similar structures and morphologies to the $Co_6Mo_6C_2$/NCRGO composite (Figures S5 and S6). In addition, $Co_6Mo_6C_2$/NCRGO with different GO amounts (0 and 2 mg mL^{-1}) are also characterized by TEM and SEM. $Co_6Mo_6C_2$/NC composite without RGO substrates (Figure S7, panels a and c) reveals that several spherical-like particles (100−200 nm in diameter) are bound together with some disordered mesopores on the surface. When increasing GO concentration to 2 mg mL^{-1}, the number of spherical particles decrease relatively and the distribution becomes uneven on GO supports, as can be seen in Figure S7, panels b and d. In that sense, Co/Mo molar ratio of 2:1 and GO loadings of 1 mg mL^{-1} are the optimum synthesis condition to obtain the pure phase $Co_6Mo_6C_2$/NCRGO composite. Moreover, high-resolution TEM (HRTEM) image (Figure 1d) demonstrates that the well-defined lattice with the spacing of 0.391 and 0.276 nm are assigned to the (220) plane and (400) plane of $Co_6Mo_6C_2$, respectively. These carbide particles with obvious lattice fringes were marked within the yellow dotted lines. The amorphous structures outside those lines must be the porous carbon derived from PPy because of the relatively low carbonization temperature. Thus, the intimate contact between the crystalline carbides nanoparticles and amorphous carbon shell further proves that $Co_6Mo_6C_2$ particles are coated by PPy-derived porous carbon. Heavy elements can be highlighted using high-angle annular dark field scanning transmission electron microscopy (HAADF-STEM). Figure 1e shows that bright spots dispersed around RGO films can be assigned to $Co_6Mo_6C_2$ particles. Energy dispersive X-ray spectroscopy (EDX) mapping images demonstrate that the distribution of Co and Mo elements are mainly focused on the particles, while C and N elements are distributed on the whole samples uniformly. These results of mapping further confirm that $Co_6Mo_6C_2$ particles are coated by porous carbon and RGO films homogeneously. Besides, EDX spectrum (Figure S8) confirms the existence of all required elements with the atomic percent of Co and Mo determined to be 8.76 and 8.37, respectively, indicating the information on the $Co_6Mo_6C_2$/NCRGO composite as well.

Nitrogen adsorption−desorption isotherm and pore size distribution of $Co_6Mo_6C_2$/NCRGO with different GO amounts are shown in Figure S9. $Co_6Mo_6C_2$/NCRGO with 1

DOI: 10.1021/acsami.7b01096
ACS Appl. Mater. Interfaces 2017, 9, 16977−16985

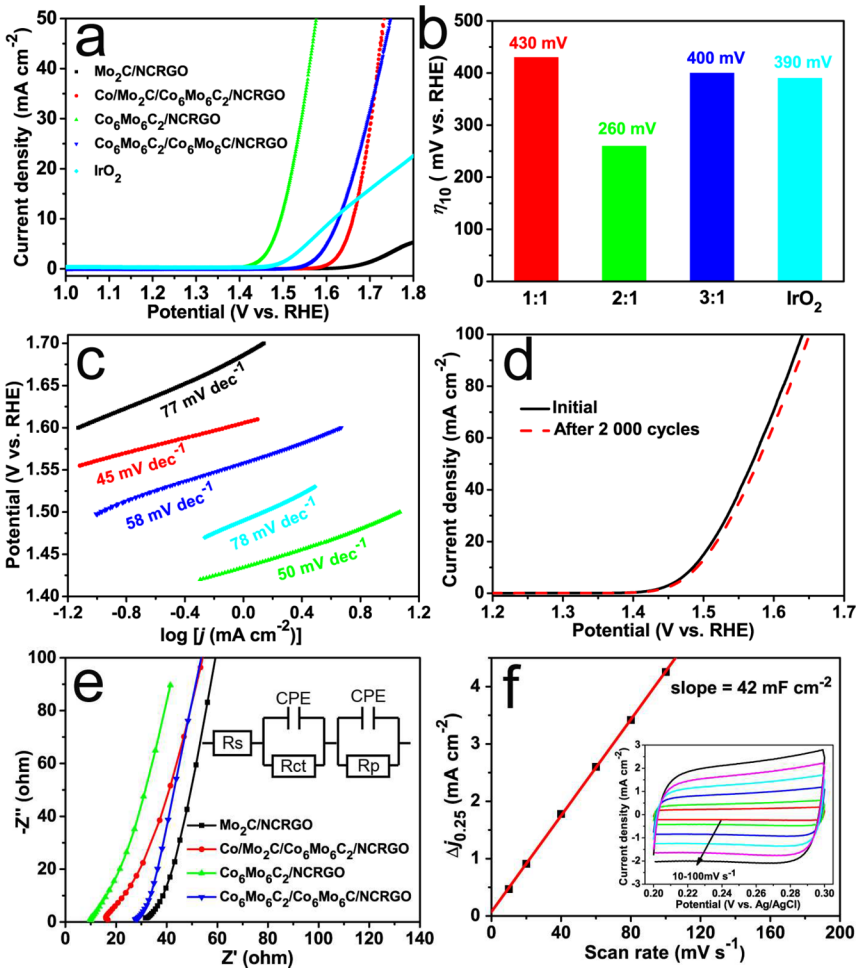

Figure 3. (a) LSV curves of Mo_2C/NCRGO, Co/Mo_2C/$Co_6Mo_6C_2$/NCRGO, $Co_6Mo_6C_2$/NCRGO, $Co_6Mo_6C_2$/Co_6Mo_6C/NCRGO, and commercial IrO_2. (b) Table for the comparison of η_{10} for corresponding samples. (c) Tafel plots for corresponding samples. (d) Cycle stability of $Co_6Mo_6C_2$/NCRGO composite before and after 2000 CV cycles. (e) EIS spectrum for corresponding samples (inset is the equivalent circuit model for fitting the EIS plots). (f) Capacitive currents of $Co_6Mo_6C_2$/NCRGO at different scan rates (10−100 mV s^{-1}). Inset is CV curves at different scan rates.

mg mL^{-1} GO loadings has the largest Brunauer−Emmett−Teller (BET) surface area of 94.1 m^2 g^{-1}, while the BET surface area of $Co_6Mo_6C_2$/NCRGO with 0 and 2 mg mL^{-1} GO loadings are 59.6 and 61.0 m^2 g^{-1}, respectively. The Barrett−Joyner−Halenda (BJH) pore size distribution shows the mesopore size of 4−5 nm. The large surface area and mesopores bring about more exposed active areas for $Co_6Mo_6C_2$/NCRGO composite, which ensure the fast electron transfer to obtain high electrocatalytic activity.

Raman spectrum of $Co_6Mo_6C_2$/NCRGO with different GO amounts (Figure S10) shows two distinct peaks at 1350 and 1591 cm^{-1}, which can be related to the D and G bands, respectively.[40] What's more, the D and G band intensity ratio (I_D/I_G) of $Co_6Mo_6C_2$/NCRGO with 0, 1, and 2 mg mL^{-1} GO amounts are 1.0, 1.17 and 1.30, respectively, indicating the high graphitic structure due to the high-temperature carbonization. The graphitization of PPy-derived porous carbon and RGO films can effectively increase the conductivity and promote the electron transfer of $Co_6Mo_6C_2$/NCRGO composite simultaneously, thus enhancing the OER performance.

The surface chemical valence state of the as-prepared composite was elucidated by X-ray photoelectron spectroscopy (XPS). The overall XPS spectrum of $Co_6Mo_6C_2$/NCRGO composite in Figure 2a suggests the existence of C, N, O, Co, Mo, and P. In Figure 2b, three deconvoluted peaks at 284.4, 285.3, and 288.3 eV are C═C/C−C, C−N, and O−C═O bonds, respectively, indicating that the major composition is sp^2-hybridized carbon. Besides, the C−N bond shows an enhanced intensity from C 1s spectrum, which indicates the high content of N-doping in porous carbon and RGO films.[41] The Mo 3d spectrum shows the mixture Mo oxidation states for $Co_6Mo_6C_2$ particles. In Figure 2c, two primary peaks at 235.3 and 232.3 eV correspond to $Mo^{6+}3d_{3/2}$ and $Mo^{6+}3d_{5/2}$, respectively, while the peak at 231.5 eV can be assigned to $Mo^{4+}3d_{3/2}$.[42] Co 2p spectrum (Figure 2d) can be deconvoluted into four main peaks. The two peaks located at 795.4 and 780.3 eV are ascribed to Co $2p_{1/2}$ and Co $2p_{3/2}$, respectively, while the two weak peaks at farther left binding energy are the shakeup satellite peaks.[43] Figure 3e gives three dominant N peaks at 398.3, 400.7, and 401.6 eV, assigned to pyridinic N, pyrrolic N, and graphitic N, respectively, suggesting that N species are incorporated in porous carbon and graphene layers. In general, the heteroatoms doping in carbon, especially N doping, can modify the electronic structures and disorder carbon structures to improve the electrocatalytic activity.[44] According to the peak area, pyridinic N dominates the main composition with the content of 57.3%, which is the most active N species in the $Co_6Mo_6C_2$/NCRGO composite.[45]

DOI: 10.1021/acsami.7b01096
ACS Appl. Mater. Interfaces 2017, 9, 16977−16985

Moreover, a small Mo 3p peak at 395.5 eV is associated with the Mo−N binding energy. The O 1s XPS spectrum containing three oxygen peaks is shown in Figure 3f. The main peak at 530.4 eV is ascribed to C−O/C═O bond, while other two peaks at 531.6 and 532.7 eV are O−N−C and C−OH bonds, respectively. These oxygen-containing groups can be attributed to a number of surface defects and oxygen vacancies, which is helpful to improve the electrochemical activity of $Co_6Mo_6C_2$/NCRGO composite. XPS spectra of Co/Mo_2C/$Co_6Mo_6C_2$/NCRGO and $Co_6Mo_6C_2$/Co_6Mo_6C/NCRGO composites also show similar chemical valence states in Figures S11 and S12, respectively.

Oxygen Evolution Reaction Activity of $Co_6Mo_6C_2$/NCRGO Composite. The incorporation of a second metal into the PCG precursor is crucial to explore the relationship between carbides composition and electrochemical activity. The OER performance was tested using a three-electrode system in 1 M KOH electrolyte at room temperature. First, $Co_6Mo_6C_2$/NCRGO composites prepared with different GO loadings (0, 1, and 2 mg mL^{-1}) (Figure S13) and different carbonization temperatures (700, 800, and 900 °C) (Figure S14) were discussed to select the optimum OER performance, that is 1 mg mL^{-1} GO amount and carbonization temperature of 800 °C. Figure 3a shows the linear sweep voltammogram (LSV) polarization curves of Co−Mo-based composites prepared with different Co/Mo molar ratios as well as the commercial IrO_2 catalyst. It is worth noting that the OER performances of Co−Mo-based composites can be improved obviously after adding Co sources into the PCG system, while Mo_2C/NCRGO composite without Co-doping shows very poor OER properties. When changing the Co/Mo molar ratios in Co-PCG precursors from 1:1 to 3:1, $Co_6Mo_6C_2$/NCRGO composite exhibits the best OER performance with a positive onset potential and a dramatic increase of current density compared with other two Co−Mo-based composites. In contrast, Co/Mo_2C/$Co_6Mo_6C_2$/NCRGO and $Co_6Mo_6C_2$/Co_6Mo_6C/NCRGO composites show a more negative onset potential, although their current density increasing trends are similar because of the excellent conductivity of carbides and RGO films. Besides, when the current density achieves 10 mA cm^{-2}, Co/Mo_2C/$Co_6Mo_6C_2$/NCRGO, $Co_6Mo_6C_2$/NCRGO, $Co_6Mo_6C_2$/Co_6Mo_6C/NCRGO, and commercial IrO_2 catalysts give the overpotential (η_{10}) of 430, 260, 400, and 390 mV versus RHE, respectively (Figure 3b). Apparently, the optimum OER electrocatalytic activity is obtained from the $Co_6Mo_6C_2$/NCRGO composite prepared with a Co/Mo molar ratio of 2:1, which has the lowest overpotential among that of other Co−Mo-based composites and commercial IrO_2 catalysts.

Tafel plots were calculated to discuss the OER kinetics of the corresponding samples. The Tafel slope of $Co_6Mo_6C_2$/NCRGO is as low as 50 mV dec^{-1}, which is much smaller than that of Mo_2C/NCRGO (77 mV dec^{-1}), $Co_6Mo_6C_2$/Co_6Mo_6C/NCRGO (58 mV dec^{-1}), and commercial IrO_2 (78 mV dec^{-1}) and is second only to Co/Mo_2C/$Co_6Mo_6C_2$/NCRGO (45 mV dec^{-1}). Moreover, the low η_{10} value and Tafel slope both indicate the extraordinary OER performance of $Co_6Mo_6C_2$/NCRGO composite, which outperforms most of the reported carbide-based catalysts and the excellent non-noble transition metal-based OER electrocatalysts in alkaline electrolytes, such as Ni/Mo_2C-PC,[30] $Fe0_{0.1}Ni_{0.9}O$,[32] and Ni−Co oxides[46] (Table S2). One major challenge for TMCs-based materials as OER electrocatalysts is the alkaline stability. The durability of $Co_6Mo_6C_2$/NCRGO composite was measured using CV method ranging from 1.3 to 1.5 V versus RHE at the scan rate of 100 mV s^{-1}. Compared with the initial one, the LSV curve of $Co_6Mo_6C_2$/NCRGO composite (Figure 3d) only has a slight shift to the smaller current density after 2000 CV cycles, which proves its outstanding OER stability.

For further study, electrochemical impedance spectroscopy (EIS) was used to examine the electrode kinetics at the electrolyte/electrocatalyst interfaces. The charge transfer resistance (R_{ct}) between the bulk electrolyte and the electrode surfaces can be calculated by fitting the EIS plots using the equivalent circuit model inset in Figure 3e. The fitted curves all match coincidentally well with the original one, suggesting that the equivalent circuit model is suitable to calculate the exact R_{ct} value (Figure S15). R_{ct} value of $Co_6Mo_6C_2$/NCRGO composite is only 9.0 Ω, comparing favorably to Mo_2C/NCRGO (64.3 Ω), Co/Mo_2C/$Co_6Mo_6C_2$/NCRGO (15.6 Ω), and $Co_6Mo_6C_2$/Co_6Mo_6C/NCRGO (13.4 Ω) (Table S1). The small R_{ct} value of $Co_6Mo_6C_2$/NCRGO composite ensures the fast faradaic process and electron transfer for OER, which is attributed to the unique porous structures and active $Co_6Mo_6C_2$ species. To estimate the electrochemical surface area (ECSA), the double-layer capacitance (C_{dl}) was measured through CV measurements at different scan rates from 10 to 100 mV s^{-1}. The potential ranged from 0.2 to 0.3 V versus Ag/AgCl without faradaic processes was selected for capacitance measurements. Although the morphologies and structures of other Co−Mo-based composites are similar to $Co_6Mo_6C_2$/NCRGO, the C_{dl} values are different distinctly but agree with their OER performance. In Figure 3f, $Co_6Mo_6C_2$/NCRGO composite has the largest C_{dl} of 42 mF cm^{-2} calculated by the slope from the linear fitting of CV curves at different scan rates. In contrast, Mo_2C/NCRGO, Co/Mo_2C/$Co_6Mo_6C_2$/NCRGO, and $Co_6Mo_6C_2$/Co_6Mo_6C/NCRGO are calculated to be 1.4, 6.7, 20 mF cm^{-2}, respectively (Figure S16). Thus, $Co_6Mo_6C_2$/NCRGO composite with pure phase bimetallic carbides has more active sites and larger ECSA than that of Co−Mo-based composites containing complex carbides compositions.

In order to prove the advantages of using POMs as a Mo source, a common Mo salt of ammonium heptamolybdate tetrahydrate ($(NH_4)_6Mo_7O_{24}\cdot 4H_2O$) was used as the replacement in the Co-PCG precursor to prepare the $Co_6Mo_6C_2$/NCRGO-1 composite. The XRD pattern of the $Co_6Mo_6C_2$/NCRGO-1 composite (Figure S17) shows the similar $Co_6Mo_6C_2$ phase peaks to the sample prepared using PMo_{12} as a Mo source. In Figure S18a, the TEM image of the $Co_6Mo_6C_2$/NCRGO-1 composite shows the rodlike morphology with a diameter of about 2 μm decorated with little RGO films on the edge. Similarly, the SEM image (Figure S18b) exhibits that polymerized PPy particles piled into rodlike morphology in the micron scale, while crumpled RGO films are coated on the surface of the rod randomly. In general, when the alkali metal ions (e.g., NH^{4+}) replace H^+ of POMs, the redox ability of these POMs would decrease obviously. Thus, the redox ability of $(NH_4)_6Mo_7O_{24}\cdot 4H_2O$ is weaker than PMo_{12}, which cannot ensure the in situ polymerization of PPy on RGO films uniformly. The severe agglomeration morphology of the $Co_6Mo_6C_2$/NCRGO-1 composite obviously demonstrates that using PMo_{12} as Mo sources in the Co-PCG precursor plays the critical role to prepare nanoparticles anchored on RGO films uniformly. Afterward, the effects of different Mo sources on OER performance were studied for comparison by LSV and Tafel measurement. Accordingly, the $Co_6Mo_6C_2$/NCRGO-1 composite reflects a more negative overpotential of 345 mV

DOI: 10.1021/acsami.7b01096
ACS Appl. Mater. Interfaces 2017, 9, 16977−16985

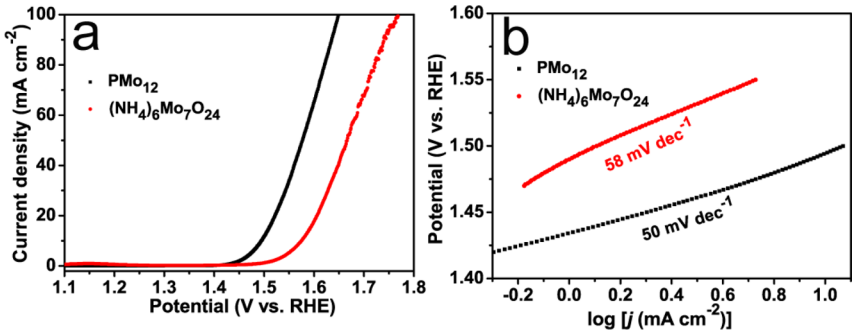

Figure 4. (a) LSV curves and (b) Tafel slope of $Co_6Mo_6C_2$/NCRGO composites using different Mo precursors.

versus RHE at 10 mA cm^{-2} and a larger Tafel slope of 58 mV dec^{-1} than the best performed $Co_6Mo_6C_2$/NCRGO using PMo_{12} as Mo sources (Figure 4, panels a and b). In brief, the large-scaled rod-like morphology with severe agglomerated structures using $(NH_4)_6Mo_7O_{24}\cdot 4H_2O$ as Mo sources could be the main reason that leads to the inferior OER performance of the $Co_6Mo_6C_2$/NCRGO-1 composite.

On the basis of the above results, the superior OER catalytic performance of $Co_6Mo_6C_2$/NCRGO composite can be ascribed to the following reasons: (1) $Co_6Mo_6C_2$ nanoparticles with high electrical conductivity are the main active species with intrinsically metallic conductivity for OER. (2) $Co_6Mo_6C_2$ nanoparticles coated by PPy-derived N-doped porous carbon enable it to prevent the direct contact with the harsh electrolytes and avoid the corrosion in the alkaline media, which makes the long-term stability of $Co_6Mo_6C_2$/NCRGO during the OER electrocatalytic process. (3) N species doping in PPy-derived porous carbon lattice and RGO films can induce more defects and graphitization to provide rich active sites and enhance the charge transfer capacity. (4) RGO films as conductive supports enable the fast charge/mass transfer and favorable reaction kinetics because of the low charge transfer resistance. In that sense, $Co_6Mo_6C_2$/NCRGO composite with distinct structures is expected to provide large surface area, efficient electron transfer, and rich accessible catalytic sites for OER performance.

4. CONCLUSION

In summary, we report here the $Co_6Mo_6C_2$/NCRGO composite derived from the Co-PCG precursors as the efficient electrocatalyst for OER. Controlling the Co/Mo molar ratios in Co-PCG precursors is of great importance to prepare pure phase $Co_6Mo_6C_2$ nanoparticles. The unique structure of Co-PCG precursor makes sure that the morphology and structure of the as-prepared $Co_6Mo_6C_2$/NCRGO composite remain unchanged with the small-sized particles encapsulated in PPy-derived porous carbon and grown on RGO supports uniformly. In the alkaline medium, the $Co_6Mo_6C_2$/NCRGO composite shows highly electrocatalytic activity for OER, with a low overpotential of 260 mV versus RHE at 10 mA cm^{-2}, a small Tafel slope of 50 mV dec^{-1}, and excellent stability. Therefore, the as-prepared bimetallic carbides-based composite can be the desired OER electrocatalyst as the replacement of the commercial noble metal based catalysts in industrial production. Further synthesis and exploration of the transition metal-based bimetallic carbides will provide a promising avenue toward efficient OER electrocatalysts and even the overall water splitting.

■ ASSOCIATED CONTENT

Supporting Information

The Supporting Information is available free of charge on the ACS Publications website at DOI: 10.1021/acsami.7b01096.

Structure and morphology characterizations including XRD, TEM, SEM, EDX, Raman, XPS, and N_2 adsorpotion-desorpotion isotherm for $Co_6Mo_6C_2$@NCRGO and other control samples in Figures S1−S12, S17, and S18. LSV curves, Tafel plots, EIS spectra, and CV curves for $Co_6Mo_6C_2$@NCRGO and other control samples in Figures S13−S16. Impedance parameter comparison in Table S1 and literature comparison in Table S2 (PDF)

■ AUTHOR INFORMATION

Corresponding Authors

*E-mail: slli@njnu.edu.cn.
*E-mail: yqlan@njnu.edu.cn.

ORCID

Long-Zhang Dong: 0000-0002-9276-5101
Ya-Qian Lan: 0000-0002-2140-7980

Author Contributions

‡Y.-J.T. and C.-H. L. contributed equally to this work.

Notes

The authors declare no competing financial interest.

■ ACKNOWLEDGMENTS

This work was financially supported by the National Natural Science Foundation of China (Grants 21622104, 21371099, and 21471080), the NSF of Jiangsu Province of China (Grant BK20141445), the doctor dissertation subject funding project of Nanjing Normal University (Grant YXXT16_013), the Priority Academic Program Development of Jiangsu Higher Education Institutions and the Foundation of Jiangsu Collaborative Innovation Center of Biomedical Functional Materials.

■ REFERENCES

(1) Walter, M. G.; Warren, E. L.; McKone, J. R.; Boettcher, S. W.; Mi, Q.; Santori, E. A.; Lewis, N. S. Solar Water Splitting Cells. *Chem. Rev.* **2010**, *110*, 6446−6473.

(2) Lewis, N. S. Research Opportunities to Advance Solar Energy Utilization. *Science* **2016**, *351*, 353−363.

(3) McCrory, C. C. L.; Jung, S.; Ferrer, I. M.; Chatman, S. M.; Peters, J. C.; Jaramillo, T. F. Benchmarking Hydrogen Evolving Reaction and Oxygen Evolving Reaction Electrocatalysts for Solar Water Splitting Devices. *J. Am. Chem. Soc.* **2015**, *137*, 4347−4357.

DOI: 10.1021/acsami.7b01096
ACS Appl. Mater. Interfaces 2017, 9, 16977−16985

(4) Du, P.; Eisenberg, R. Catalysts Made of Earth-Abundant Elements (Co, Ni, Fe) for Water Splitting: Recent Progress and Future Challenges. *Energy Environ. Sci.* **2012**, *5*, 6012−6021.
(5) Hunter, B. M.; Gray, H. B.; Müller, A. M. Earth-Abundant Heterogeneous Water Oxidation Catalysts. *Chem. Rev.* **2016**, *116*, 14120−14136.
(6) Hong, W. T.; Risch, M.; Stoerzinger, K. A.; Grimaud, A.; Suntivich, J.; Shao-Horn, Y. Toward the Rational Design of Non-Precious Transition Metal Oxides for Oxygen Electrocatalysis. *Energy Environ. Sci.* **2015**, *8*, 1404−1427.
(7) Anantharaj, S.; Ede, S. R.; Sakthikumar, K.; Karthick, K.; Mishra, S.; Kundu, S. Recent Trends and Perspectives in Electrochemical Water Splitting with an Emphasis on Sulfide, Selenide, and Phosphide Catalysts of Fe, Co, and Ni: A Review. *ACS Catal.* **2016**, *6*, 8069−8097.
(8) Parent, A. R.; Crabtree, R. H.; Brudvig, G. W. Comparison of Primary Oxidants for Water-Oxidation Catalysis. *Chem. Soc. Rev.* **2013**, *42*, 2247−2252.
(9) Ma, T. Y.; Dai, S.; Jaroniec, M.; Qiao, S. Z. Metal−Organic Framework Derived Hybrid Co_3O_4-Carbon Porous Nanowire Arrays as Reversible Oxygen Evolution Electrodes. *J. Am. Chem. Soc.* **2014**, *136*, 13925−13931.
(10) Gorlin, Y.; Lassalle-Kaiser, B.; Benck, J. D.; Gul, S.; Webb, S. M.; Yachandra, V. K.; Yano, J.; Jaramillo, T. F. In Situ X-ray Absorption Spectroscopy Investigation of a Bifunctional Manganese Oxide Catalyst with High Activity for Electrochemical Water Oxidation and Oxygen Reduction. *J. Am. Chem. Soc.* **2013**, *135*, 8525−8534.
(11) Li, C.; Han, X.; Cheng, F.; Hu, Y.; Chen, C.; Chen, J. Phase and Composition Controllable Synthesis of Cobalt Manganese Spinel Nanoparticles Towards Efficient Oxygen Electrocatalysis. *Nat. Commun.* **2015**, *6*, 7345−7352.
(12) Song, F.; Hu, X. Exfoliation of Layered Double Hydroxides for Enhanced Oxygen Evolution Catalysis. *Nat. Commun.* **2014**, *5*, 4477−4485.
(13) Tang, C.; Wang, H.-S.; Wang, H.-F.; Zhang, Q.; Tian, G.-L.; Nie, J.-Q.; Wei, F. Spatially Confined Hybridization of Nanometer-Sized NiFe Hydroxides into Nitrogen-Doped Graphene Frameworks Leading to Superior Oxygen Evolution Reactivity. *Adv. Mater.* **2015**, *27*, 4516−4522.
(14) Stern, L.-A.; Feng, L.; Song, F.; Hu, X. Ni_2P as a Janus Catalyst for Water Splitting: the Oxygen Evolution Activity of Ni_2P Nanoparticles. *Energy Environ. Sci.* **2015**, *8*, 2347−2351.
(15) Ryu, J.; Jung, N.; Jang, J. H.; Kim, H.-J.; Yoo, S. J. In Situ Transformation of Hydrogen-Evolving CoP Nanoparticles: Toward Efficient Oxygen Evolution Catalysts Bearing Dispersed Morphologies with Co-oxo/hydroxo Molecular Units. *ACS Catal.* **2015**, *5*, 4066−4074.
(16) Li, D.; Baydoun, H.; Verani, C. N.; Brock, S. L. Efficient Water Oxidation Using CoMnP Nanoparticles. *J. Am. Chem. Soc.* **2016**, *138*, 4006−4009.
(17) Freemantle, M. Carbides Catalyze Methane Reforming. *Chem. Eng. News* **1997**, *75*, 5.
(18) Mellinger, Z. J.; Kelly, T. G.; Chen, J. G. Pd-Modified Tungsten Carbide for Methanol Electro-oxidation: From Surface Science Studies to Electrochemical Evaluation. *ACS Catal.* **2012**, *2*, 751−758.
(19) Kok Poh, C.; Hua Lim, S.; Tian, Z.; Lai, L.; Ping Feng, Y.; Shen, Z.; Lin, J. Pt-W_xC Nano-Composites as an Efficient Electrochemical Catalyst for Oxygen Reduction Reaction. *Nano Energy* **2013**, *2*, 28−39.
(20) Li, Z.; Ji, S.; Pollet, B. G.; Shen, P. K. A Co_3W_3C Promoted Pd Catalyst Exhibiting Competitive Performance Over Pt/C Catalysts Towards the Oxygen Reduction Reaction. *Chem. Commun.* **2014**, *50*, 566−568.
(21) Hu, Y.; Jensen, J. O.; Zhang, W.; Cleemann, L. N.; Xing, W.; Bjerrum, N. J.; Li, Q. Hollow Spheres of Iron Carbide Nanoparticles Encased in Graphitic Layers as Oxygen Reduction Catalysts. *Angew. Chem., Int. Ed.* **2014**, *53*, 3675−3679.
(22) Liu, Y.; Mustain, W. E. Structural and Electrochemical Studies of Pt Clusters Supported on High-Surface-Area Tungsten Carbide for Oxygen Reduction. *ACS Catal.* **2011**, *1*, 212−220.
(23) Chen, W. F.; Wang, C. H.; Sasaki, K.; Marinkovic, N.; Xu, W.; Muckerman, J. T.; Zhu, Y.; Adzic, R. R. Highly Active and Durable Nanostructured Molybdenum Carbide Electrocatalysts for Hydrogen Production. *Energy Environ. Sci.* **2013**, *6*, 943−951.
(24) Liu, Y.; Yu, G.; Li, G.-D.; Sun, Y.; Asefa, T.; Chen, W.; Zou, X. Coupling Mo_2C with Nitrogen-Rich Nanocarbon Leads to Efficient Hydrogen-Evolution Electrocatalytic Sites. *Angew. Chem., Int. Ed.* **2015**, *54*, 10752−10757.
(25) Wan, C.; Regmi, Y. N.; Leonard, B. M. Multiple Phases of Molybdenum Carbide as Electrocatalysts for the Hydrogen Evolution Reaction. *Angew. Chem.* **2014**, *126*, 6525−6528.
(26) Li, J.-S.; Wang, Y.; Liu, C.-H.; Li, S.-L.; Wang, Y.-G.; Dong, L.-Z.; Dai, Z.-H.; Li, Y.-F.; Lan, Y.-Q. Coupled Molybdenum Carbide and Reduced Graphene Oxide Electrocatalysts for Efficient Hydrogen Evolution. *Nat. Commun.* **2016**, *7*, 11204−11211.
(27) Ma, F.-X.; Wu, H. B.; Xia, B. Y.; Xu, C.-Y.; Lou, X. W. Hierarchical β-Mo_2C Nanotubes Organized by Ultrathin Nanosheets as a Highly Efficient Electrocatalyst for Hydrogen Production. *Angew. Chem., Int. Ed.* **2015**, *54*, 15395−15399.
(28) Xu, K.; Ding, H.; Lv, H.; Chen, P.; Lu, X.; Cheng, H.; Zhou, T.; Liu, S.; Wu, X.; Wu, C.; Xie, Y. Dual Electrical-Behavior Regulation on Electrocatalysts Realizing Enhanced Electrochemical Water Oxidation. *Adv. Mater.* **2016**, *28*, 3326−3332.
(29) Su, J.; Xia, G.; Li, R.; Yang, Y.; Chen, J.; Shi, R.; Jiang, P.; Chen, Q. Co_3ZnC/Co Nano Heterojunctions Encapsulated in N-doped Graphene Layers Derived from PBAs as Highly Efficient Bi-Functional OER and ORR Electrocatalysts. *J. Mater. Chem. A* **2016**, *4*, 9204−9212.
(30) Yu, Z.-Y.; Duan, Y.; Gao, M.-R.; Lang, C.-C.; Zheng, Y.-R.; Yu, S.-H. A One-Dimensional Porous Carbon-Supported Ni/Mo_2C Dual Catalyst for Efficient Water Splitting. *Chem. Sci.* **2017**, *8*, 968−973.
(31) Lin, H.; Liu, N.; Shi, Z.; Guo, Y.; Tang, Y.; Gao, Q. Cobalt-Doping in Molybdenum-Carbide Nanowires Toward Efficient Electrocatalytic Hydrogen Evolution. *Adv. Funct. Mater.* **2016**, *26*, 5590−5598.
(32) Fominykh, K.; Chernev, P.; Zaharieva, I.; Sicklinger, J.; Stefanic, G.; Döblinger, M.; Müller, A.; Pokharel, A.; Böcklein, S.; Scheu, C.; Bein, T.; Fattakhova-Rohlfing, D. Iron-Doped Nickel Oxide Nanocrystals as Highly Efficient Electrocatalysts for Alkaline Water Splitting. *ACS Nano* **2015**, *9*, 5180−5188.
(33) Wan, C.; Leonard, B. M. Iron-Doped Molybdenum Carbide Catalyst with High Activity and Stability for the Hydrogen Evolution Reaction. *Chem. Mater.* **2015**, *27*, 4281−4288.
(34) Zou, X.; Su, J.; Silva, R.; Goswami, A.; Sathe, B. R.; Asefa, T. Efficient Oxygen Evolution Reaction Catalyzed by Low-Density Ni-Doped Co_3O_4 Nanomaterials Derived from Metal-Embedded Graphitic C_3N_4. *Chem. Commun.* **2013**, *49*, 7522−7524.
(35) Wu, G.; Santandreu, A.; Kellogg, W.; Gupta, S.; Ogoke, O.; Zhang, H.; Wang, H.-L.; Dai, L. Carbon Nanocomposite Catalysts for Oxygen Reduction and Evolution Reactions: From Nitrogen Doping to Transition-Metal Addition. *Nano Energy* **2016**, *29*, 83−110.
(36) Liu, C.-H.; Tang, Y.-J.; Wang, X.-L.; Huang, W.; Li, S.-L.; Dong, L.-Z.; Lan, Y.-Q. Highly Active Co-Mo-C/NRGO Composite as Efficient Oxygen Electrode for Water-Oxygen Redox Cycle. *J. Mater. Chem. A* **2016**, *4*, 18100−18106.
(37) Hill, C. L. Introduction: Polyoxometalates Multicomponent Molecular Vehicles To Probe Fundamental Issues and Practical Problems. *Chem. Rev.* **1998**, *98*, 1−2.
(38) Kovtyukhova, N. I.; Ollivier, P. J.; Martin, B. R.; Mallouk, T. E.; Chizhik, S. A.; Buzaneva, E. V.; Gorchinskiy, A. D. Layer-by-Layer Assembly of Ultrathin Composite Films from Micron-Sized Graphite Oxide Sheets and Polycations. *Chem. Mater.* **1999**, *11*, 771−778.
(39) Alconchel, S.; Sapina, F.; Martinez, E. From Nitrides to Carbides: Topotactic Synthesis of the η-Carbides Fe_3Mo_3C and Co_3Mo_3C. *Dalton Trans.* **2004**, 2463−2468.
(40) Qu, K.; Zheng, Y.; Dai, S.; Qiao, S. Z. Graphene Oxide-Polydopamine Derived N, S-Codoped Carbon Nanosheets as Superior Bifunctional Electrocatalysts for Oxygen Reduction and Evolution. *Nano Energy* **2016**, *19*, 373−381.

DOI: 10.1021/acsami.7b01096
ACS Appl. Mater. Interfaces 2017, 9, 16977−16985

(41) Zhang, Z.; Qin, Y.; Dou, M.; Ji, J.; Wang, F. One-Step Conversion from Ni/Fe Polyphthalocyanine to N-Doped Carbon Supported Ni-Fe Nanoparticles for Highly Efficient Water Splitting. *Nano Energy* **2016**, *30*, 426−433.
(42) Tang, Y.-J.; Wang, Y.; Wang, X.-L.; Li, S.-L.; Huang, W.; Dong, L.-Z.; Liu, C.-H.; Li, Y.-F.; Lan, Y.-Q. Molybdenum Disulfide/Nitrogen-Doped Reduced Graphene Oxide Nanocomposite with Enlarged Interlayer Spacing for Electrocatalytic Hydrogen Evolution. *Adv. Energy Mater.* **2016**, *6*, 1600116−1600122.
(43) Zeng, M.; Liu, Y.; Zhao, F.; Nie, K.; Han, N.; Wang, X.; Huang, W.; Song, X.; Zhong, J.; Li, Y. Metallic Cobalt Nanoparticles Encapsulated in Nitrogen-Enriched Graphene Shells: Its Bifunctional Electrocatalysis and Application in Zinc−Air Batteries. *Adv. Funct. Mater.* **2016**, *26*, 4397−4404.
(44) Lahaye, J.; Nansé, G.; Bagreev, A.; Strelko, V. Porous Structure and Surface Chemistry of Nitrogen Containing Carbons from Polymers. *Carbon* **1999**, *37*, 585−590.
(45) Li, Q.; Pan, H.; Higgins, D.; Cao, R.; Zhang, G.; Lv, H.; Wu, K.; Cho, J.; Wu, G. Metal−Organic Framework-Derived Bamboo-like Nitrogen-Doped Graphene Tubes as an Active Matrix for Hybrid Oxygen-Reduction Electrocatalysts. *Small* **2015**, *11*, 1443−1452.
(46) Wang, H.-Y.; Hsu, Y.-Y.; Chen, R.; Chan, T.-S.; Chen, H. M.; Liu, B. Ni^{3+}-Induced Formation of Active NiOOH on the Spinel Ni−Co Oxide Surface for Efficient Oxygen Evolution Reaction. *Adv. Energy Mater.* **2015**, *5*, 1500091−1500098.

DOI: 10.1021/acsami.7b01096
ACS Appl. Mater. Interfaces 2017, 9, 16977−16985